JOURNAL OF GEOPHYSICAL RESEARCH, VOL. 111, D15201, doi:10.1029/2005JD006312, 2006

Click Here for Full Article

Climatic effects of different aerosol types in China simulated by the UCLA general circulation model

Y. Gu,[1] K. N. Liou,[1] Y. Xue,[1] C. R. Mechoso,[1] W. Li,[2] and Y. Luo[3]

Received 1 June 2005; revised 8 February 2006; accepted 9 March 2006; published 1 August 2006.

[1] The climatic effects of various types of aerosol in China have been investigated by using the atmospheric general circulation model (AGCM) developed at the University of California, Los Angeles (UCLA). The model includes an efficient and physically based radiation parameterization scheme specifically developed for application to clouds and aerosols. Simulation results show that inclusion of a background aerosol optical depth of 0.2 reduces the global mean net surface solar flux by about 5 W m^{-2} and produces a decrease in precipitation in the tropics as a result of decreased temperature contrast between this area and the middle to high latitudes, which suppresses tropical convection. These decreases have partially corrected the overestimates in the surface solar flux and precipitation in the UCLA AGCM simulations without the aerosol effect. The experiment with increased aerosol optical depths in China shows a noticeable increase in precipitation in the southern part of China in July due to the cooling in the midlatitudes that leads to the strengthening of the Hadley circulation. Aerosol types play an important role in the determination of the global mean radiation budget and regional climate. While sulfates mainly reflect solar radiation and induce negative forcing at the surface, black carbon and large dust particles absorb substantial solar radiation and have a positive solar forcing at the top of the atmosphere, but reduce the solar radiation reaching the surface. Large dust particles also have a significant effect on thermal IR radiation under clear conditions, but this effect is largely masked by clouds generated from the model in AGCM simulations. Black carbon and large dust particles in China would heat the air column in the middle to high latitudes and tend to move the simulated precipitation inland, i.e., toward the Himalayas. The inclusion of black carbon in our simulations has not produced the ''north drought/south flooding'' precipitation pattern that has frequently occurred in China during the past 50 years.

Citation: Gu, Y., K. N. Liou, Y. Xue, C. R. Mechoso, W. Li, and Y. Luo (2006), Climatic effects of different aerosol types in China simulated by the UCLA general circulation model, *J. Geophys. Res.*, *111*, D15201, doi:10.1029/2005JD006312.

1. Introduction

[2] Climate and climate change greatly affect human society and are of common concerns to people across national and regional boundaries. At the same time, human activities in turn play an important role in climate change. There is a growing consensus that uncertainties in quantifying the aerosol effects on climate, both direct and indirect, must be reduced through a combination effort involving observational and modeling studies.

[3] Atmospheric aerosols affect climate through the scattering and absorption of solar radiation (direct effect) and through their influence on cloud formation (indirect effect). Simple radiation energy balance models have been used to assess the impact of stratospheric or tropospheric aerosols on global climate through their effect on cloud optical properties and the global mean surface temperature [e.g., *Charlock and Sellers*, 1980; *Harshvardhan et al.*, 1984]. The radiative forcing of aerosols has been studied by a number of scientists using GCMs [e.g., *Boucher and Anderson*, 1995; *Pan et al.*, 1997; *Penner et al.*, 1998]. The effects of aerosols on the Earth's environment and climate have become an important scientific issue [*Mitchell et al.*, 1995].

[4] The assessment of direct aerosol climate impact has mostly been limited to a certain aerosol type such as volcanic aerosols [*Pollack et al.*, 1993], soil dust [*Miller and Tegen*, 1998], mineral dust [*Tegen and Lacis*, 1996], and black carbon [*Menon et al.*, 2002]. *Menon et al.* [2002] investigated the direct radiative effect of aerosols in China and a part of India using the observed aerosol optical depths in these regions based on a climate model. They reported that absorbing black carbon could significantly influence the large-scale circulation and hydrologic cycle and hence regional climate and suggested that the composition specificity of aerosols is needed to comprehend climatic effects.

[1]Department of Atmospheric and Oceanic Sciences, University of California, Los Angeles, Los Angeles, California, USA.
[2]Chinese Academy of Meteorological Sciences, Beijing, China.
[3]National Natural Science Foundation of China, Beijing, China.

Copyright 2006 by the American Geophysical Union.
0148-0227/06/2005JD006312$09.00

[5] Since aerosols stem from local sources, it would be important to investigate the effect of an extremely polluted area such as those occurring in China on climate and climate modeling. *Giorgi et al.* [2002] carried out a series of simulations using a coupled regional climate-chemistry/aerosol model to assess the radiative forcing and surface climate effects of anthropogenic sulfate and fossil fuel soot over East Asia. Their results showed that anthropogenic sulfate induces a negative radiative forcing at the top of the atmosphere (TOA) with maximum negative values of up to -8 and -15 W m^{-2} in winter and summer, respectively. Fossil fuel soot, on the other hand, exerts a positive TOA radiative forcing of 0.5 to 2 W m^{-2}. Using a regional climate model developed in China, *Wu et al.* [2004] reported that black carbon aerosols induce a positive radiative forcing at TOA and a negative forcing at the surface. In this study, we investigate the effects of different types of aerosol locally produced in China on climate and climate change through the atmospheric general circulation and their interaction with other physical processes. China is the largest underdeveloping country in the world and has been obtaining 80% of its energy from coal combustion. The coal production in China during 1990 was about 5 times larger than that of 1960 [*Sun et al.*, 1997]. While China has achieved an impressive advance in its economic development since the 1980s, one of the major costs of this advance has been the severe increase in the atmospheric pollution due to emission of a large volume of smoke containing SO_2, which can be transformed into sulfate and black carbon aerosols in air [*Lefohn et al.*, 1999; *Xu*, 2001]. These aerosols have impacted not only the local environment and public health, but also the regional climate, even in remote locations. For example, a case study in 2000 reported that the dust from China affects the solar radiation resource in the United States [*Gueymard et al.*, 2000], which could then alter the regional atmospheric circulation and contribute to regional climate change.

[6] Our objective in this study is to investigate the effect of different types of aerosols in China, a heavily polluted region, on climate by examining the responses of the climate system to direct aerosol radiative forcings in the University of California, Los Angeles atmospheric general circulation model (UCLA AGCM) in terms of the cloud, radiation, temperature, precipitation, and general circulation patterns. We start in section 2 by describing the model employed and its radiation parameterization for aerosols, followed by a description of the observed aerosol optical depth data in China and the experiment design in section 3. The model simulations and discussions are presented in section 4. Conclusions are given in section 5.

2. Model Description and Radiation Parameterization

2.1. UCLA AGCM

[7] The present UCLA AGCM is a state-of-the-art grid point model of the global atmosphere extending from the Earth's surface to a height of 50 km. This model has been successfully applied to a number of climate studies, including El Niño/Southern Oscillation and the Asian Monsoon [e.g., *Arakawa*, 2000; *Mechoso et al.*, 2000]. Recently, a more physically based radiation scheme has been incorporated in the UCLA AGCM to enhance its capability for studies of a variety of climate problems, including aerosol effects [*Gu et al.*, 2003]. The prognostic variables of the UCLA AGCM are the horizontal wind, potential temperature, water vapor mixing ratio, cloud liquid water and cloud ice water, planetary boundary layer (PBL) depth, surface pressure, land surface temperature, and snow depth over land. The PBL is parameterized as a well-mixed layer of the variable depth [*Li et al.*, 2002]. Parameterization of the cumulus convection and its interaction with the PBL follows *Pan and Randall* [1998]. The geographical distribution of sea surface temperature is prescribed based on a 31 year (1960–1990) climatology corresponding to the GISST version 2.2 data set [*Rayner et al.*, 1995]. The sea ice thickness and extent as well as the surface albedo and roughness length are prescribed [*Alexander and Mobley*, 1976; *Dorman and Sellers*, 1989]. Ozone mixing ratios are prescribed as a function of latitude, height, and time based on a 1985–1990 climatology [*Li and Shine*, 1995]. In this study, we have used a low-resolution model version with a grid size covering 4° latitude by 5° longitude and with a vertical layer of 15 layers from the Earth's surface to the top at 1 hPa. More details on the UCLA AGCM can be found at http://www.atmos.ucla.edu/~mechoso/esm.

2.2. Radiation Parameterization for Aerosols

[8] The radiation calculation in the UCLA AGCM version that we used is based on the Fu-Liou scheme. A combination of the delta-four-stream approximation for solar flux calculations [*Liou et al.*, 1988] and delta-two/four-stream approximation for IR flux calculations [*Fu et al.*, 1997] is employed in the model to assure both accuracy and efficiency. The incorporation of nongray gaseous absorption in multiple-scattering atmospheres is based on the correlated *k*-distribution method developed by *Fu and Liou* [1992]. Parameterization of the single-scattering properties for cloud particles is implemented by following the procedure developed by *Fu and Liou* [1993]. The spectral extinction coefficient, the single-scattering albedo, and the asymmetry factor are parameterized in terms of the prognostic ice/liquid water content and the particle effective radius, which is fixed at 10 μm for water clouds and 80 μm for ice clouds. To increase computational accuracy, we apply the similarity principle for radiative transfer to each grid point to account for the fractional energy in the diffraction peak of the phase function. The solar and IR spectra are divided into 6 and 12 bands, respectively, according to the location of absorption bands. Using the correlated *k*-distribution method, 121 spectral radiation calculations are required for each vertical profile in the AGCM. In conjunction with the radiation parameterization, we have also incorporated a cloud fraction overlap scheme. We define the fractional cloudiness (C_f) by linear interpolation in $\log_{10} q_t$ between $q_t = 10^{-10}$ kg kg^{-1} corresponding to the upper limit of cloud free condition ($C_f = 0$) and $q_t = 10^{-5}$ kg kg^{-1} corresponding to overcast condition ($C_f = 1$), where q_t is the predicted total water mixing ratio. Producing partial cloudiness introduces the cloud vertical overlap problem, which is an important issue in climate model studies. Various parameterizations of the cloud overlap effect have been developed, and several AGCM sensitivity tests have been performed [e.g., *Liang and Wang*, 1997;

Chou et al., 1998; *Gu and Liou*, 2001]. The most common methods used in contemporary AGCMs are random overlap [*Manabe and Strickler*, 1964] and maximum/random overlap [*Geleyn and Hollingsworth*, 1979; *Chou et al.*, 1998]. The latter has been shown to be more consistent with the observed cloud distribution [*Tian and Curry*, 1989]. Here we employ the method of maximum/random overlap, in which clouds are divided into three types according to their heights: low, middle, and high. Maximum overlap is used for clouds of the same type, while random overlap is subsequently employed for clouds of different types. Scaling of the optical depth in groups of clouds of the same type is performed in terms of cloud cover based on the method developed by *Chou et al.* [1998]. An atmospheric column, therefore, can be divided into at most 8 sectors if clouds are present in all of the three groups. Radiation calculations can then be performed for each of the cloud configurations, and the all-sky flux can be determined as the weighted sum of the flux computed for each sector.

[9] The radiative properties of atmospheric aerosols, including the extinction coefficient, single-scattering albedo, and asymmetry factor, must be determined from their composition, shape, and size distribution. Many AGCMs to date either neglect the effect of aerosols or simply prescribe average values for their optical properties in the calculations. For example, *Menon et al.* [2002] used a single-scattering albedo value of 0.85 for the aerosol composition involving 85% sulfate and 15% black carbon, and a value of 1 for pure sulfate, for all wavelengths. Some model studies used specific aerosol types, such as volcanic aerosols, desert aerosols, or aerosols produced by biomass burning [e.g., *Pollack et al.*, 1993].

[10] Aerosols in the atmosphere are assumed to be a mixture of different components, referred to as aerosol types. In the radiation scheme for the present UCLA AGCM, a total of 18 aerosol types have been parameterized by using the Optical Properties of Aerosols and Clouds (OPAC) database [*d'Almeida et al.*, 1991; *Tegen and Lacis*, 1996; *Hess et al.*, 1998]. These aerosol types include maritime, continental, urban, five different sizes of mineral dust, insoluble, water soluble, soot (black carbon), sea salt in two modes (accumulation mode and coarse mode), mineral dust in four different modes (nucleation mode, accumulation mode, coarse mode, and transported mode), and sulfate droplets. The database provides the single-scattering properties for spherical aerosols computed from the Lorenz-Mie theory, in which the humidity effects are accounted for. In the current radiation scheme for the UCLA AGCM, the single-scattering properties of the 18 aerosol types for 60 wavelengths in the spectral region between 0.3 μm and 40 μm are interpolated into the Fu-Liou spectral bands. These properties are vertically distributed and dependent on the aerosol type and relative humidity.

[11] Atmospheric aerosols generally contain a mixture of several components. For example, soot particles may be internally or externally mixed with nonabsorbing materials, resulting in fairly different absorption properties [*Martins et al.*, 1998]. *Hansen and Nazarenko* [2004] indicated that while external mixing has been conventionally used, internal mixing increases the black carbon absorption by a factor of two, leading to a better agreement with empirical data. However, they also pointed out that substantial uncertainty exists. Using the GISS GCM-II coupled to a mixed layer ocean model, *Chung and Seinfeld* [2005] reported that anthropogenic black carbon tends to raise global and annual average surface air temperatures by about 0.2°K if external mixing is assumed but by about 0.37°K if internal mixing is used; the climate sensitivity of black carbon direct radiative forcing, however, is independent of the assumption of its mixing state. In our study, we have followed the external mixture scheme in which the total aerosol optical depth is the sum of individual optical depths. Up to three aerosol constituents are allowed in the scheme and hence enable us to examine the aerosol climate effect under various compositions. In this study, we focus on three aerosol types: (1) sulfates produced by atmospheric chemical reactions from gaseous precursors such as SO_2 from the natural production through volcanic eruptions, and the anthropogenic source such as coal burning and traffic; (2) black carbon or soot, produced by incomplete combustion from coal, biomass burning, biofuel, etc. (the emission of black carbon has been especially large in China due to the low-temperature household burning of coal and biofuels [*Streets et al.*, 2001]); and (3) mineral dust aerosols, of which an amount up to 30 to 50% originated from anthropogenic activities [*Tegen and Fung*, 1995]. Because mineral dust particles are relatively large and can be lifted to high altitudes in the troposphere, they may exert an important thermal IR radiative forcing, a topic that has been neglected in most aerosol radiative forcing studies.

[12] Aerosol composition measurements in China have been reported in several studies. *He et al.* [2001] collected weekly $PM_{2.5}$ samples at two sites in Beijing from July 1999 to September 2000 and reported that organic carbon (OC) was the most abundant, constituting more than 30% of the total $PM_{2.5}$ mass at both sites, while ammonium, nitrate and sulfate accounted for about 25–30%. Conducting a 1-month field sampling campaign in the Yangtze delta region of China during November 1999, *Xu et al.* [2002] showed that OC is the dominant species (~50% of the $PM_{2.5}$ mass), followed by sulfate and nitrate. An experiment using the observed aerosol compositions would be certainly more realistic in determining the aerosol radiative forcing in GCM simulations. However, it would be difficult to conduct such an experiment simply because the spectral single-scattering property data for OC are not available at this time. Moreover, measurements of the aerosol composition in China have only been carried out at very limited sites for a relatively short period. Information of the spatial distribution and composition of different types of aerosols is insufficient for incorporation in GCM studies.

[13] For this reason, we have performed a number of simulations to examine the aerosol direct radiative forcing based on prescribed compositions, which are representative of the observed aerosol radiative properties determined from the Indian Ocean Experiment carried out by *Ramanathan et al.* [2001]. It should be noted that the direct radiative forcing of aerosols is actually determined by their single-scattering properties. Using integrated observations from satellite, aircraft, ships, surface stations, and balloons, *Ramanathan et al.* [2001] reported that black carbon contributed about 11% to the visible optical depth of the Indo-Asian aerosols, and the single-scattering albedo estimated by several independent methods was consistently around 0.9 both inland

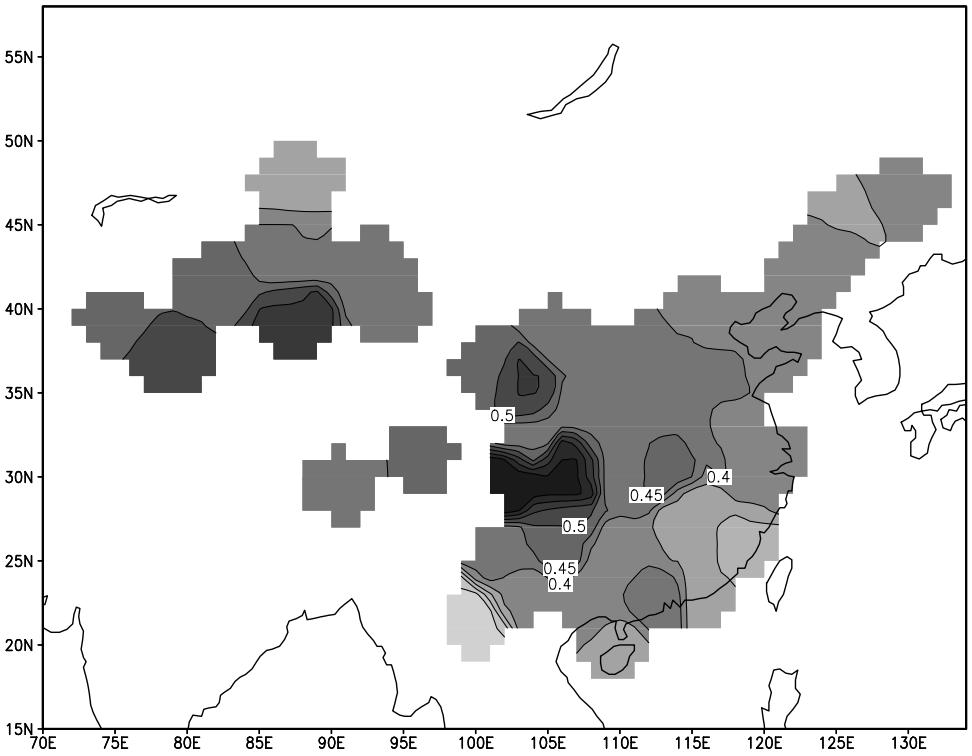

Figure 1. Observed annual mean aerosol optical depth in China.

and over the open ocean. On the basis of these observations, we have chosen 90% of the maritime type in the experiments AERO and CHIN to represent the background aerosols, and added 10% BC aerosols based on the observed data of 11% to approximate the effect of combustion processes. The combination of these aerosol types gives a single-scattering albedo of about 0.9 that is the observed value determined from the Indian Ocean Experiment. In a previous climate experiment, *Menon et al.* [2002] used a single-scattering albedo of 0.85 to represent the aerosol composition measurement reported by *Ramanathan et al.* [2001].

3. Observed Aerosol Data in China and Experiment Design

[14] In this study, we employ the aerosol data collected by scientists in China during the past 40 years to investigate the effects of the aerosols in China on climatic temperature and precipitation distributions. The yearly and monthly mean aerosol optical depths at the wavelength of 0.75 μm over China have been determined from the data involving the daily direct solar radiation, sunshine duration, surface pressure, and vapor pressure from 1961 to 1990 [*Luo et al.*, 2001]. As an example, Figure 1 shows the observed annual mean aerosol optical depth. The larger aerosol optical depths are found in the southern China with a maximum value of about 0.7.

[15] The global climatology of aerosol optical depth has become available in recent years. The Total Ozone Mapping Spectrometer (TOMS) has provided global aerosol optical depth for more than 10 years [*Torres et al.*, 1998, 2002]. The monthly averaged aerosol optical depths from TOMS over China are much larger than those obtained in sites during the last 40 years by a factor of 2–3. The Moderate Resolution Imaging Spectroradiometer (MODIS) on board Terra and Aqua satellites has been mapping the aerosol optical depth over the oceans globally and a portion of the continents since 2000 and 2002, respectively [*Remer et al.*, 2002; *Chu et al.*, 2002]. The Multi-angle Imaging SpectroRadiometer (MISR) on board Terra also provides 5 year data for the aerosol parameters [*Diner et al.*, 2001]. The global climatology of aerosol optical depth derived from long observational record of the Advanced Very High Resolution Radiometer (AVHRR) radiance measurements appears to be systematically lower than those from the MODIS and MISR results due to the potentially imperfect differentiation between clouds and optically thick aerosols, and the differences in the cloud screening approaches [*Geogdzhayev et al.*, 2004].

[16] In view of the available satellite data for aerosol optical depth climatology and in order to be compatible and consistent with the long-term surface observations in China, we use a background aerosol optical depth of 0.2 for areas outside China in AGCM simulations to focus our analysis on the effect of localized aerosols on regional climate patterns. This selection is in part based on the averaged aerosol optical depth derived from the TOMS observations for regions (e.g., Southern Hemisphere) relatively free of the effect of anthropogenic aerosols [*Torres et al.*, 2002].

[17] In accordance with our research objective, i.e., to investigate the extent to which a significant loading of atmospheric aerosols in China affects the cloud structure, temperature, and precipitation patterns, particularly over China and the surrounding regions, six experiments have been performed by using the updated UCLA AGCM described above. The effect of greenhouse gases and other

Table 1. Experiment Design

Experiment	Aerosol Optical Depth	Aerosol Composition
CTRL	0.0	none
AERO	background aerosol optical depth of 0.2 globally	90% maritime; 10% soot
CHIN	observed aerosol optical depths at the wavelength of 0.75 μm over China; background aerosol optical depth of 0.2 for the area other than China	90% maritime; 10% soot
SULF	same as CHIN	90% sulfate; 10% soot
DUST	same as CHIN	90% 8.0 μm dust; 10% soot
SOOT	same as CHIN	100% soot

forcings are fixed in all experiments so that aerosols are the only forcing in this study. A summary of the climate experiments are described below and shown in Table 1.

[18] 1. The first experiment is a control run (CTRL) in which the aerosol effect has been excluded from the model simulation.

[19] 2. In the second experiment, AERO, the aerosol effect is accounted for by incorporating a background aerosol optical depth of 0.2, consisting of 90% maritime aerosols and 10% black carbon.

[20] 3. The third experiment, CHIN, is identical to the second, except that the aerosol optical depth observation available in China is used to replace the background aerosol optical depth in that area.

[21] 4–6. The fourth (SULF), fifth (DUST), and sixth (SOOT) experiments are similar to the third, except that different aerosol types are assumed. SULF uses 90% sulfate and 10% soot, while DUST and SOOT involve 90% mineral dust and 10% soot, and 100% soot, respectively, to mimic the air pollution condition in China.

4. Model Simulations

4.1. Off-line Aerosol Radiative Forcing

[22] Prior to the AGCM simulations, we examined the off-line radiative effect of different aerosol types. The solar and IR radiative forcings produced by various aerosol types at the TOA and the surface are given in Table 2. The aerosol optical depth is set to 0.2 and the atmospheric profile used represents the midlatitude summer condition. The input aerosol optical depth represents the vertically integrated column value, which has been distributed vertically according to a certain weighting profile based on the layer pressure and scale height, a height at which the aerosol loading is reduced to e^{-1} of the surface value, which is set to be 3 km in this study. The aerosol loading decreases exponentially and the highest aerosol layer in the model is placed at 15 km [*Charlock et al.*, 2004]. Consequently, the spectral single-scattering properties are dependent on height according to aerosol type and relative humidity. The aerosols were assumed to be spherical in shape, an assumption that is not applicable to dust and black carbon and is a subject requiring further study. In order to identify the aerosol radiative effect, the clear condition was assumed in the calculations to exclude the cloud forcing. In the experiments, the cosine of the solar zenith angle of 0.5 and a surface albedo of 0.1 were used.

[23] As shown in Table 2, the solar radiative forcing at TOA is negative for a few types of aerosols including maritime, sulfate and small mineral dust particles, which scatter solar radiation with little absorption produced. These aerosols have single-scattering albedos of almost 1.00 for the first few solar bands. Black carbon with a single-scattering albedo of about 0.2 or less in the visible, on the other hand, absorbs a substantial solar flux and leads to a positive forcing at TOA, while reduces the solar flux reaching the surface by about 100 W m^{-2}. Larger dust particles have an averaged single-scattering albedo of about 0.7 (in the visible) and produce both scattering and significant absorption of the solar radiation, resulting in a positive radiative forcing at TOA but negative at the surface. As shown in Table 2, dust particles produce a significant IR radiative forcing in addition to their effect on solar radiative transfer.

4.2. Aerosol Climate Effect

[24] We first evaluate the direct radiative effect of aerosols by comparing the 5 year simulation results of the

Table 2. Solar and IR Radiative Forcing for Different Aerosol Types at the Top of Atmosphere (TOA) and the Surface (SFC)

	Net Solar Forcing, W m^{-2}		Net IR Forcing, W m^{-2}	
Aerosol Type	TOA	SFC	TOA	SFC
Maritime	−17.6	−19.4	4.0	4.3
Sulfate	−16.0	−16.5	0.0	0.7
Black carbon	18.5	−100.2	0.0	0.5
0.5 μm mineral dust	−23.1	−37.9	0.7	0.9
2.0 μm mineral dust	−10.7	−51.2	7.1	7.3
8.0 μm mineral dust	6.4	−64.6	10.1	9.3

Table 3. Global Mean Differences in Precipitation, Total Cloud Cover, Surface Air Temperature, and Planetary Albedo Between the Experiments AERO and CTRL and CHIN and AERO for the January and July Simulations

	AERO−CTRL	CHIN−AERO
Precipitation, mm d^{-1}		
Jan	−0.34	0.0037
Jul	−0.33	0.0016
Cloud cover, %		
Jan	−2.13	−0.09
Jul	−1.98	0.13
Surface air temperature, °K		
Jan	0.02	−0.01
Jul	0.18	0.26
Planetary albedo, %		
Jan	−0.29	−0.18
Jul	−0.80	−0.84

Table 4. Global Mean Solar and IR Radiative Forcing With Respect to CTRL in July for Different Aerosol Experiments at the TOA and the SFC

	Net Solar Forcing, W m^{-2}		Net IR Forcing, W m^{-2}		Net Radiative Forcing, W m^{-2}	
Experiment	TOA	SFC	TOA	SFC	TOA	SFC
AERO	2.42	−5.10	2.80	3.18	5.22	−1.92
CHIN	2.56	−5.13	2.95	3.51	5.51	−1.62
SULF	2.31	−7.65	1.16	1.72	3.47	−5.93
DUST	21.71	−10.80	−1.63	11.87	20.08	1.07
SOOT	30.97	−18.28	−5.95	10.59	25.02	−7.69

designed experiments AERO and CTRL as described above using the updated UCLA AGCM. We have compared the 5 year and the last 3 year mean simulation results. The differences between the two are insignificant. For example, the relative difference between the two means for the net solar radiative flux at TOA was only about 0.12%. For this reason, results are presented in terms of the 5 year means. The global means of the major climate parameters including

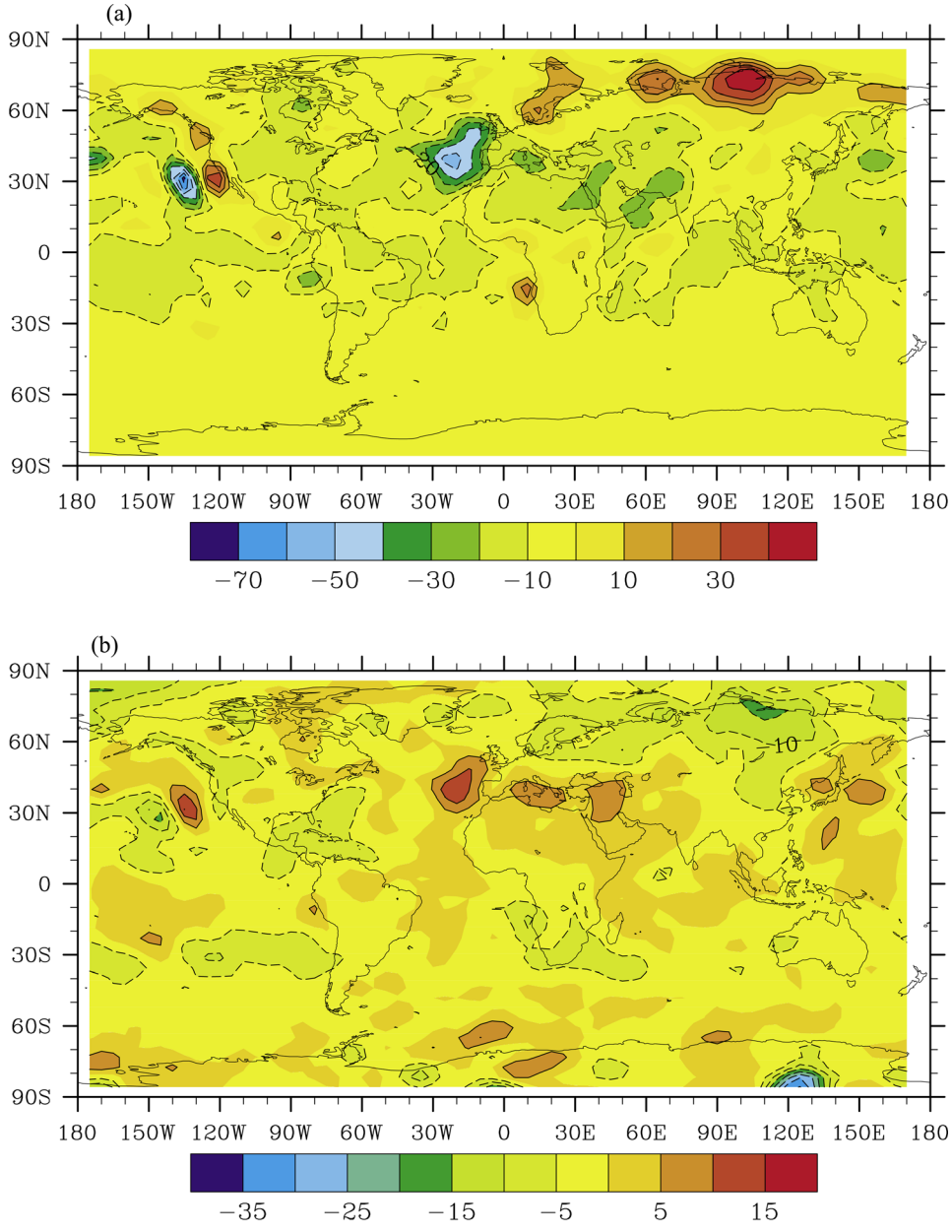

Figure 2. Differences in the July mean (a) net surface solar fluxes (W m^{-2}) and (b) cloud cover (%) between the experiments AERO and CTRL.

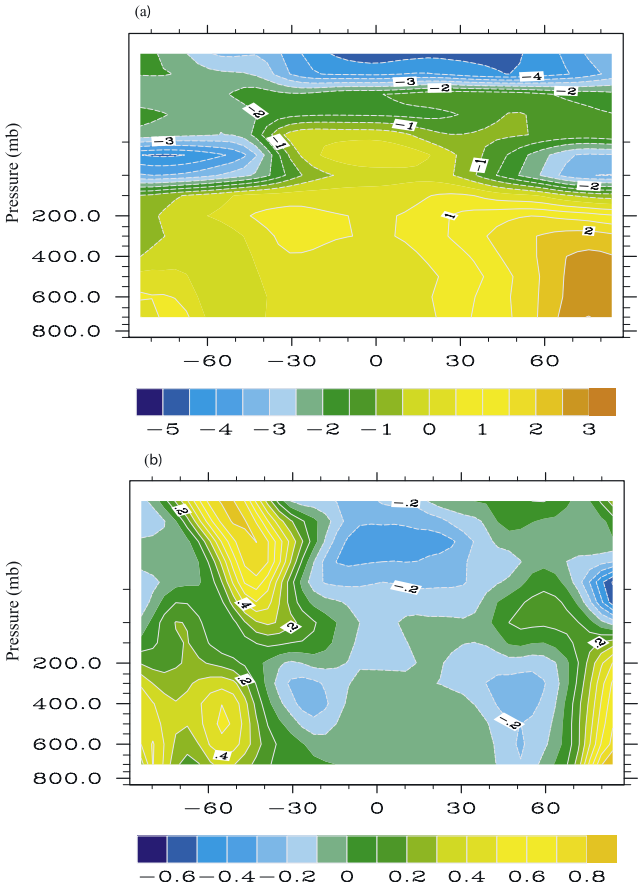

Figure 3. Differences in the July zonal mean temperature (°K) between experiments (a) AERO and CTRL and (b) CHIN and AERO.

precipitation, total cloud cover, surface air temperature and planetary albedo are shown in Table 3. In Table 4, we display the July global mean solar, IR, and net radiative forcings at TOA and the surface for the five aerosol experiments with respect to the control run (CTRL). The radiative forcings for January have similar results and are not shown. It is seen that the total cloudiness simulation in AERO is smaller than that in CTRL by about 2.0% for both January and July (Table 3). Reduction in total cloudiness in the AERO experiment is consistent with the positive solar forcing at TOA, as shown in Table 4. The global mean value of precipitation is reduced by about 0.34 mm d^{-1} and 0.33 mm d^{-1} in January and July, respectively. The corresponding outgoing longwave radiation (OLR) is reduced by about 2.8 W m^{-2} with a positive IR forcing at TOA (Table 4), despite the fact that the cloud amount decreases. This is produced by the positive IR forcing of maritime aerosols, as shown in Table 2. The planetary albedo is reduced by 0.29% (Table 3) as a result of reduced cloudiness, leading to a positive solar forcing at the TOA (Table 4). The solar forcing at the surface is negative with a global mean value of about −5 W m^{-2}, indicating a decrease in the solar insolation at the surface associated with scattering and absorption of solar radiation by aerosols. This decrease along with the reduction in precipitation has corrected overestimates in the surface solar flux and precipitation of about 15 W m^{-2} and 0.34–0.4 mm d^{-1}, respectively, in the UCLA AGCM simulations without inclusion of the direct aerosol radiative effect [*Gu et al.*, 2003]. The global surface temperature is slightly increased in July (Table 3) as a result of absorption by the 10% soot aerosols, the positive IR forcing at the surface produced by maritime aerosols, and reduced latent heat associated with reduction in precipitation. The effects of aerosols on solar radiative fluxes at TOA and the surface are larger in July than in January. However, the precipitation and cloud differences are slightly larger in January than those in July as a result of the aerosol-radiation-cloud interaction. The differences between AERO and CTRL are statistically significant at 95% level according to the t-test. Note that the results shown here have been obtained on the basis of the AERO simulation in which 90% maritime and 10% soot aerosols were used. The effect of aerosol type on climate simulations will be delineated in section 4.4.

[25] We next examine the geographic distribution of the differences in the July mean net surface solar flux between the AERO and CTRL simulations (Figure 2a). Including aerosols, the simulated results illustrate decreases in solar flux at the Earth's surface in the tropics and midlatitudes of the Northern Hemisphere, except along the west coast of North America, and increases in high latitudes. Note that the differences are mainly located in the Northern (summer) Hemisphere in association with the position of the sun. The most remarkable area of positive values is extended from North Europe to North Asia, while maximum negative values are found in the midlatitude east Atlantic Ocean. Differences in the distribution of surface solar flux could be explained by the changes in cloudiness. Figure 2b shows the differences in cloud cover between the AERO and CTRL simulations. Increasing (decreasing) surface solar flux generally corresponds to reduced (enhanced) cloudiness, leading to less (more) reflected solar flux and hence larger (smaller) solar flux reaching the surface. The zonal mean temperature differences between AERO and CTRL are displayed in Figure 3a. Warming is seen in the entire troposphere in the high latitudes of the Northern Hemisphere, in association with increased solar insolation. Reduction of cloud water is also found in the lower troposphere in the high latitudes of Northern Hemisphere (not shown).

[26] Figure 4 shows the simulated July mean precipitation and OLR changes. Inclusion of aerosols yields decreased precipitation in areas including the ITCZ, the East Asian summer monsoon, and over Central America and Africa. The largest reduction is over Arabian Ocean and north of the Bay of Bengal, partially offset by an increase to the north of the decreasing area. Two other precipitation dipoles are found in the Central America and along the west coast of Africa (Figure 4a) associated with the decreased temperature contrast between the tropical area and the middle to high latitudes as shown in Figure 3a. Note that warming over the land of lower latitudes or increase in the land/ocean temperature gradient normally results in increased monsoon rainfall. However, warming over the middle to high latitudes (inner lands) will weaken the Hadley circulation and suppress the tropical convection leading to precipitation reduction. The corresponding OLR shows increases in these areas, indicating decreased convection over the region with reduced precipitation (Figure 4b). Reduced OLR is seen over

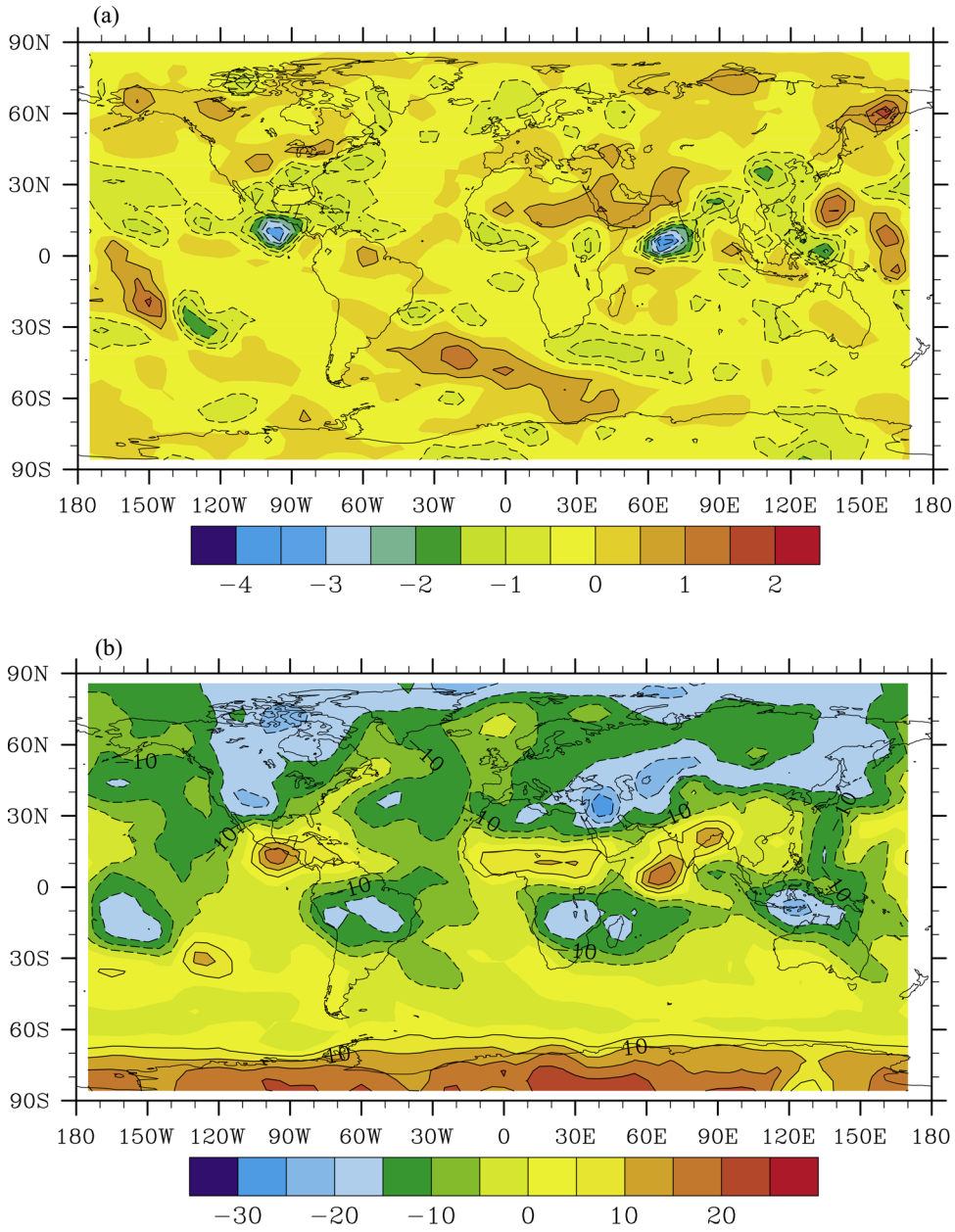

Figure 4. Differences in the July mean (a) precipitation (mm d^{-1}) and (b) outgoing longwave radiation (OLR) (W m^{-2}) between the experiments AERO and CTRL.

most of the summer northern middle and high latitudes due to the positive IR forcing produced by maritime aerosols. Increase in OLR in the South Pole is associated with the thermal emission of aerosols. Confidence levels for the cloud cover, OLR, and precipitation differences are depicted in Figure 5. The confidence level typically exceeds 95% corresponding to changes in the three fields. Anomalies are shown to be significant in all areas at above 70% level.

[27] Note that in the AERO experiment, the aerosol optical depth and type used are globally uniform, and the aerosol indirect effect is not accounted for. The preceding differences in geographic precipitation distribution patterns, therefore, are not directly related to the aerosol radiative effect, but associated with the interaction and feedback among aerosol, radiation, and cloud fields which are modulated by the direct aerosol radiative forcing and in turn affect the simulated climate.

4.3. Effect of Aerosols in China on Regional Climate

[28] The effect of the aerosol optical depth in China can be examined by comparison between the following two experiments: CHIN and AERO, in which the only difference is that the observed aerosol optical depths in China were used in CHIN. Table 3 shows differences in the global mean values of precipitation, cloudiness, surface temperature, and planetary albedo between CHIN and AERO. Inclusion of the observed aerosol optical depth in China leads to insignificant changes in the global mean values of climate parameters. However, a reduction in the planetary albedo of about 0.84% is shown in July, accompanying by an increase in the TOA net global

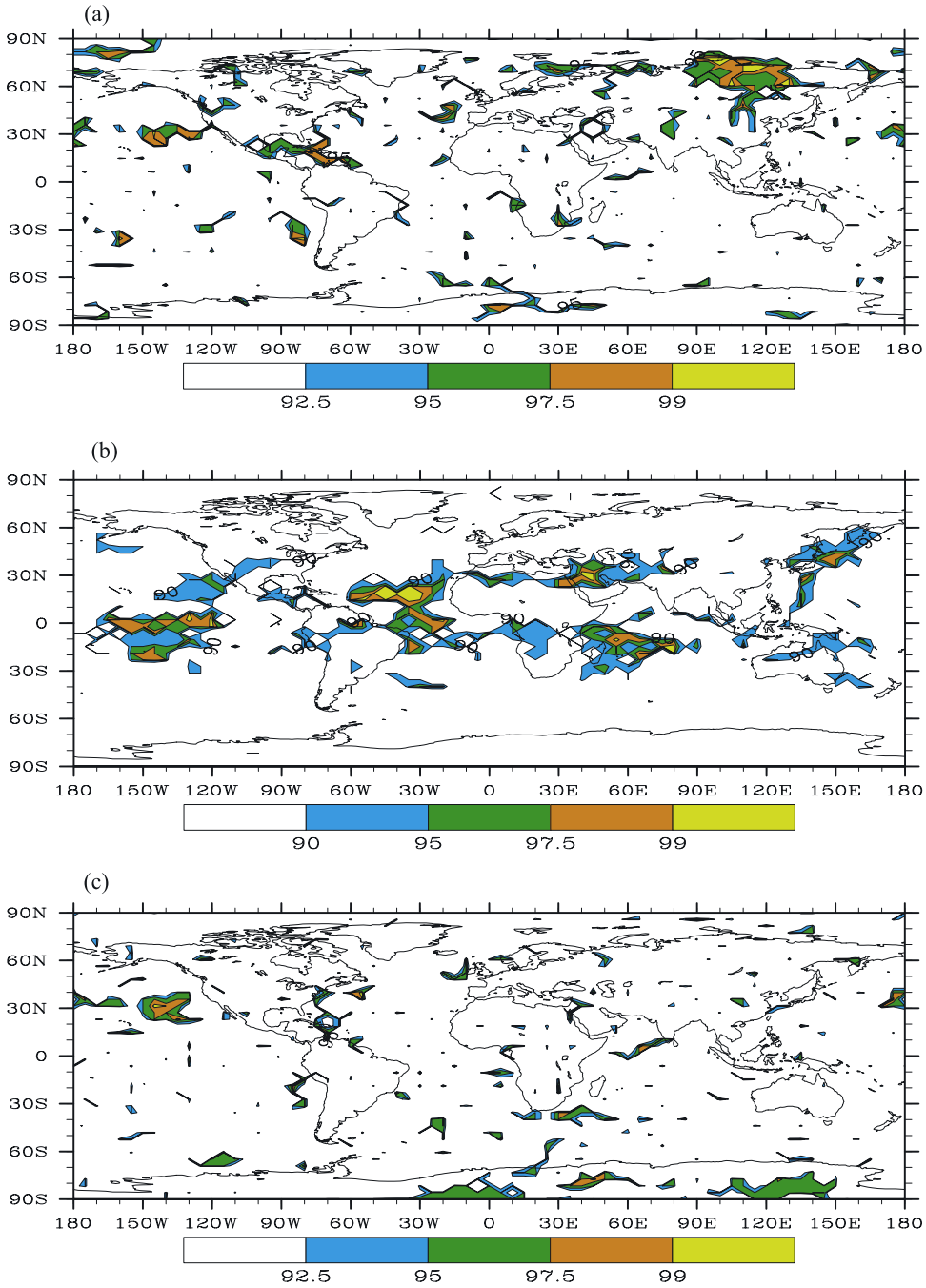

Figure 5. Significance of differences between AERO and CTRL in July mean (a) cloud cover, (b) OLR, and (c) precipitation computed by a student's t-test.

solar flux of about 0.14 W m^{-2} (Table 4). This change is primarily associated with the enhanced scattering and absorption in the atmosphere due to the use of observed aerosol optical depths in China. Increase in the surface temperature (Table 3) in July is primarily due to the enhanced positive IR forcing of 0.33 W m^{-2} (CHIN with respect to AERO) at the surface (Table 4) associated with the radiative forcings of maritime and soot aerosols (Table 2).

[29] We next examine the regional climate response to the increased aerosols in China. Since the differences between CHIN and AERO are mainly located in the summer hemisphere associated with the position of the sun, results are presented in terms of the July means. Figure 6 illustrates the distribution of the differences in the net surface solar radiation and cloudiness over Asian and West Pacific area in longitudes between 50° and 160°E and latitudes between 10°S and 80°N. Negative values in the surface solar fluxes are found in most part of China due to the increased scattering and absorption of solar radiation by aerosols (Figure 6a). The corresponding total cloud cover decreases in northern and western China and to the north (Figure 6b), which agrees with the observations that shows a decrease in the north from 1951 to 1994 [*Kaiser*, 1998]. The surface air temperature shows warming in northern China and the areas

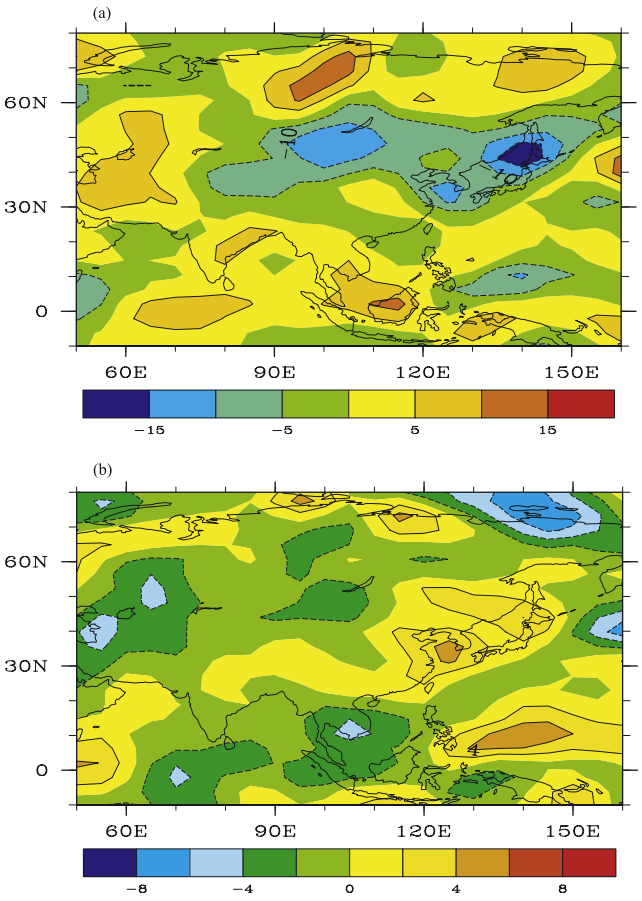

Figure 6. Differences in the July mean (a) net surface solar fluxes (W m^{-2}) and (b) cloud cover (%) between the experiments CHIN and AERO.

to the north (Figure 7) due to decreased cloud cover and enhanced surface solar insolation in these areas, associated with the inclusion of increased aerosol optical depth in China (Figure 6). The zonal mean temperature difference profile displays warming and cooling, respectively, in the high and midlatitudes in conjunction with changes in

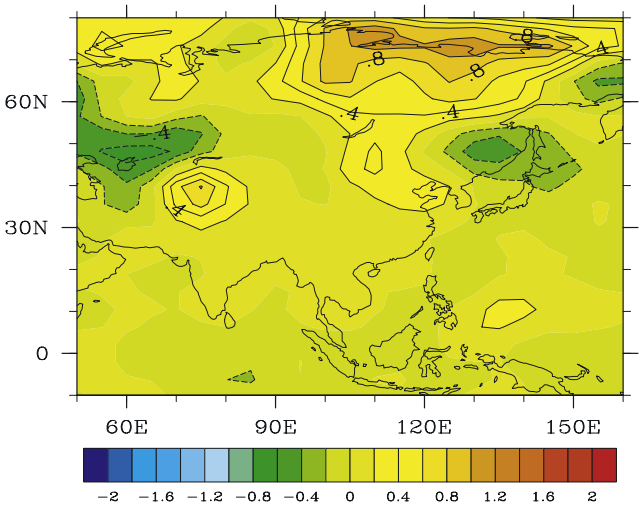

Figure 7. Differences in the July mean surface air temperature (°K) between the experiments CHIN and AERO.

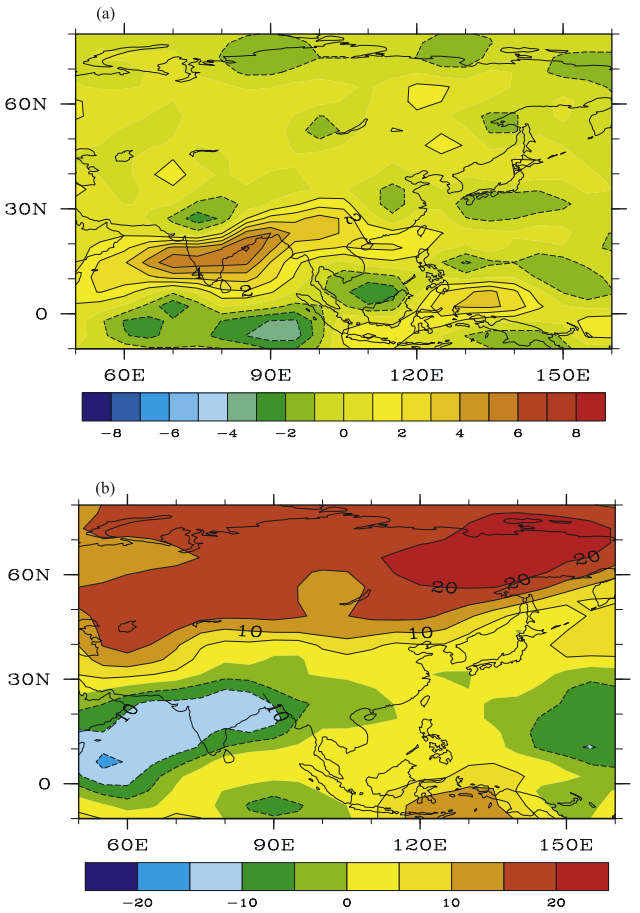

Figure 8. Differences in the July mean (a) precipitation (mm d^{-1}) and (b) OLR (W m^{-2}) between the experiments CHIN and AERO.

cloudiness (Figure 3b). Cooling in the midlatitudes strengthen the meridional circulation, resulting in increased precipitation in southern China, Arabian Sea, Bay of Bengal, as well as India and Myanmar (Figure 8a). To compensate these increases, a broad band of decreased precipitation is found to locate to the south of the increased precipitation region, with a small decrease to the north. A similar pattern has been presented by *Menon et al.* [2002]. However, since experiments CHIN and AERO employed the same aerosol types, increase in regional precipitation, especially in the southern part of China and over the Indian area where abundant moisture is available in summer, appears to be related to the increased aerosol optical depth that occurred in China. Note that *Menon et al.* [2002] suggested that increase in the precipitation in southern China could be related to increase in the absorbing aerosols, a hypothesis differs from our current finding. Positive differences in OLR are located in higher latitudes, while decreases are found to extend from North Africa to southern China where precipitation is enhanced (Figure 8b), revealing increased convection in this region.

4.4. Climate Effect of Different Types of Aerosols

[30] The off-line radiation calculations show that various types of aerosols present different radiative forcings. In this section we examine the effect of different types of aerosols

Table 5. Global Mean Differences in Precipitation, Total Cloud Cover, Surface Air Temperature, and Planetary Albedo Between the Experiments SULF/DUST/SOOT and CTRL for the January and July Simulations

	SULF−CTRL	DUST−CTRL	SOOT−CTRL
Precipitation, mm d^{-1}			
Jan	−0.49	−0.84	−1.17
Jul	−0.37	−0.59	−0.89
Cloud cover, %			
Jan	−2.38	−6.86	−10.03
Jul	−2.65	−7.30	−10.44
Surface air temperature, °K			
Jan	1.12	3.03	5.59
Jul	0.57	2.13	3.96
Planetary albedo, %			
Jan	−2.11	−8.21	−11.37
Jul	−0.76	−7.13	−10.16

on climate simulations by comparing the simulation results obtained from SULF, DUST, and SOOT with those from CTRL and CHIN. Table 5 shows differences in the global means between SULF/DUST/SOOT and CTRL simulations for January and July.

[31] Sulfates mainly reflect solar radiation as discussed in section 4.1. In Table 4 we list the radiative forcing values determined from different experiments. A reduction of about 7.65 W m^{-2} in the surface solar flux in July is found in SULF, in reference to the CTRL experiment, due to the scattering of solar radiation. The global cloudiness is also reduced by more than 2%, which corresponds to a small decrease in precipitation. The scattering effect of sulfate aerosols is similar to that of maritime aerosols, and therefore the differences between SULF and CHIN are not significant. Moreover, we show in Figure 9 the differences in precipitation and surface air temperature between experiments SULF and CTRL. Sulfate aerosols produce more precipitation over India, Bay of Bengal, and southern China, while decreases in precipitation are found to the north and south as compensation (Figure 9a). The surface air temperature shows decreases off the east coast of China and increases to the north in the high latitudes (Figure 9b). The response of regional climate to sulfate aerosols resembles that to maritime aerosols since both have similar radiative properties.

[32] The effect of large dust particles on global mean solar radiation is significant. A positive solar radiative forcing is found at TOA due to absorption of solar radiation by dust aerosols (Table 4), leading to a significant decrease in planetary albedo (Table 5), unrealistic as compared to observations. The absorption exceeds the increase of surface solar radiation associated with decrease in cloud amount of about 7% (Table 5), resulting in less solar radiation reaching the surface by more than 7 W m^{-2} in July. Negative IR forcing is found at TOA for July, as compared to CTRL (Table 4). The effect of dust particles on IR radiation appears to be opposite to that presented in the off-line calculation (Table 2). The reason is that clouds become the most important modulator of IR radiation and could overshadow the aerosol contribution in AGCM simulations. To investigate this further, we run an off-line radiative forcing calculation for large dust particles identical to the experiment presented in Table 2, except that a cloud with an optical depth of 2.0 was added to the experiment. The results show that the IR forcing produced by large dust particles in the presence of cloud is reduced from about 10 W m^{-2} to about 4 W m^{-2}, a significant reduction of 6 W m^{-2}. The increase in OLR in this case is therefore associated with decrease in cloudiness, as shown in Table 5.

[33] By reducing the net surface solar radiation, which must be offset partially by reducing evaporation, dust particles may lead to a decrease in precipitation [*Ghan et al.*, 1988; *Coakley and Cess*, 1985; *Miller and Tegen*, 1998]. The global mean precipitation in experiment DUST is reduced by about 0.84 and 0.59 mm d^{-1} compared to CTRL for January and July, respectively (Table 5). The changes in July precipitation over Asian area between DUST and CHIN are shown in Figure 10a. Differences between DUST and CTRL show similar patterns and are not presented here. The maximum reduction is located over the Arabian Sea and north of the Bay of Bengal where precipitation is displaced toward the Himalayas. Figure 11a shows the corresponding perturbed temperature profile. Warming is found in the middle to high latitudes, which weakens the Hadley circulation and reduces tropical convection and precipitation. Similar results are also found in the simulations by *Miller and Tegen* [1998] in association with the effect of dust particles which increases the heating of the column over the Himalayas and hence draw the monsoon circulation further landward. Precipitation is also reduced in northern China and west Pacific Ocean. The cloud cover decreases over the regions where precipitation is reduced (Figure 10c), resulting in more solar radiation reaching the

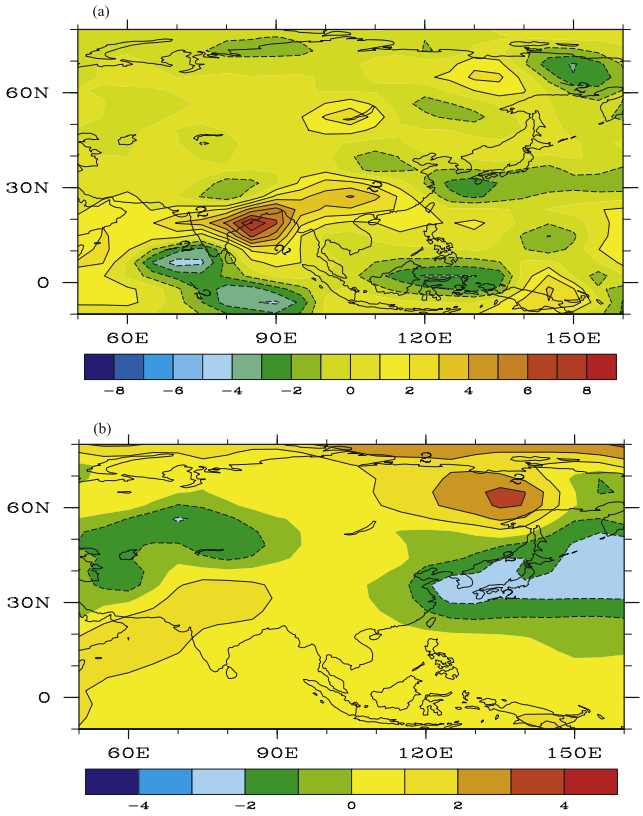

Figure 9. Differences in the July mean (a) precipitation (mm d^{-1}) and (b) surface air temperature (°K) between experiments SULF and CTRL.

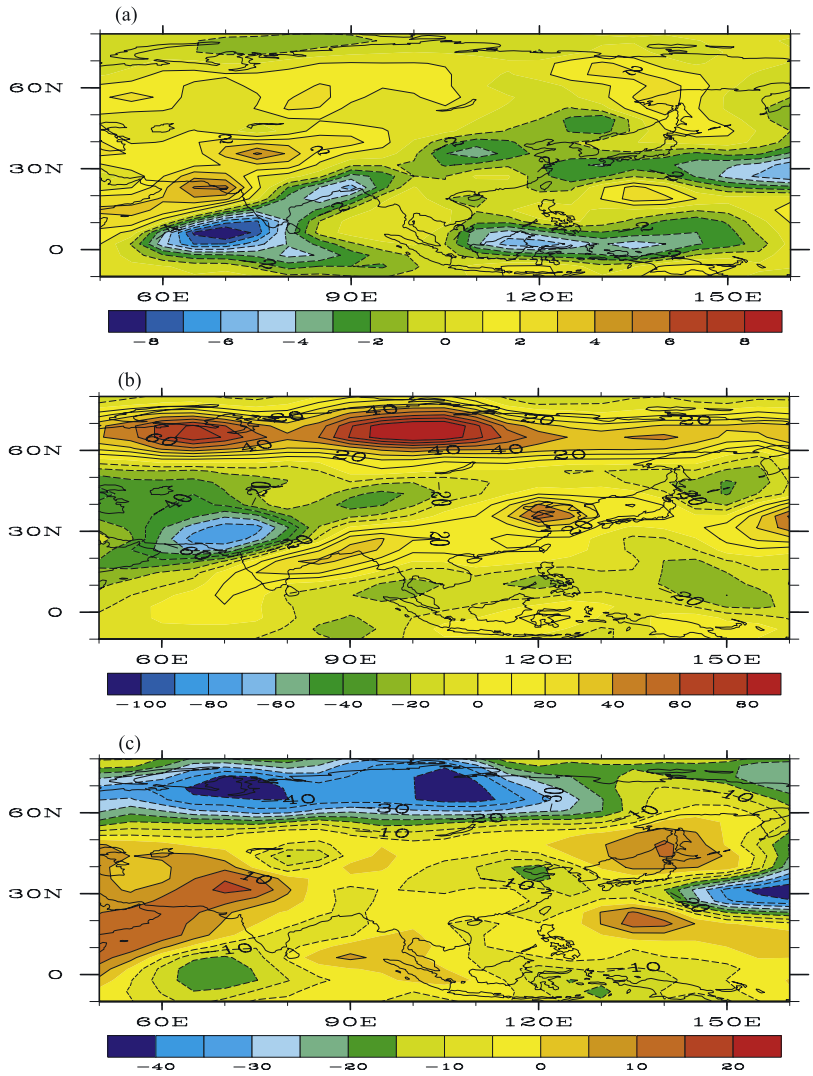

Figure 10. Differences in the July mean (a) precipitation (mm d^{-1}), (b) net surface solar fluxes (W m^{-2}), and (c) cloud cover (%) between experiments DUST and CHIN.

surface in these area (Figure 10b). Cloud cover is also reduced in the high latitudes with increased net surface solar radiation.

[34] The black carbon absorbs substantial solar radiation and has significant effects on solar radiation. With the inclusion of 100% black carbon aerosols in the simulation, OLR is enhanced by about 6 W m^{-2} in July simulations as compared to CTRL (Table 4) due to a reduction in the total cloud cover of about 10% (Table 5), a result of the interaction among aerosol, radiation, and cloud fields. Similar to large dust particles, a positive solar radiative forcing is seen at TOA in the experiment SOOT (Table 4), corresponding to a large decrease in the planetary albedo (Table 5). Net solar radiation at the surface decreases by about 18 W m^{-2} in the July simulations because of the substantial absorption of solar flux by black carbon, which exceeds increase in the surface solar radiation associated with the reduced cloud cover simulated from the model. These results are in good agreement with those reported by *Giorgi et al.* [2002] and *Wu et al.* [2004].

[35] The July surface air temperature differences between simulations SOOT and CHIN are shown in Figure 12a. These differences appear primarily in the summer hemisphere corresponding to the solar insolation distribution. Warming is generally found in the Northern Hemisphere with a maximum located at the North Pole and a global mean increase in temperature of about 4°K in July (Table 5), indicating that black carbon aerosol has a significant global warming effect, as compared to the maritime aerosols used in CHIN. None of the other types of aerosols produces similar surface air temperature difference patterns (e.g., Figure 9b). Using the Goddard Institute for Space Studies (GISS) climate model, *Hansen and Nazarenko* [2004] found that soot is twice as potent as carbon dioxide in raising global surface air temperatures in the Arctic and the Northern Hemisphere by speeding up the melting of snow and sea ice. The results from the current study regarding the effect of soot aerosols on surface air temperature based on the UCLA AGCM simulation are in excellent agreement with their findings.

[36] Similar to dust particles which also absorb substantial solar radiation, a precipitation dipole north of Bay of Bengal is found in the simulation including soot, where rain is displaced toward Himalayas (Figure 12b). The precipita-

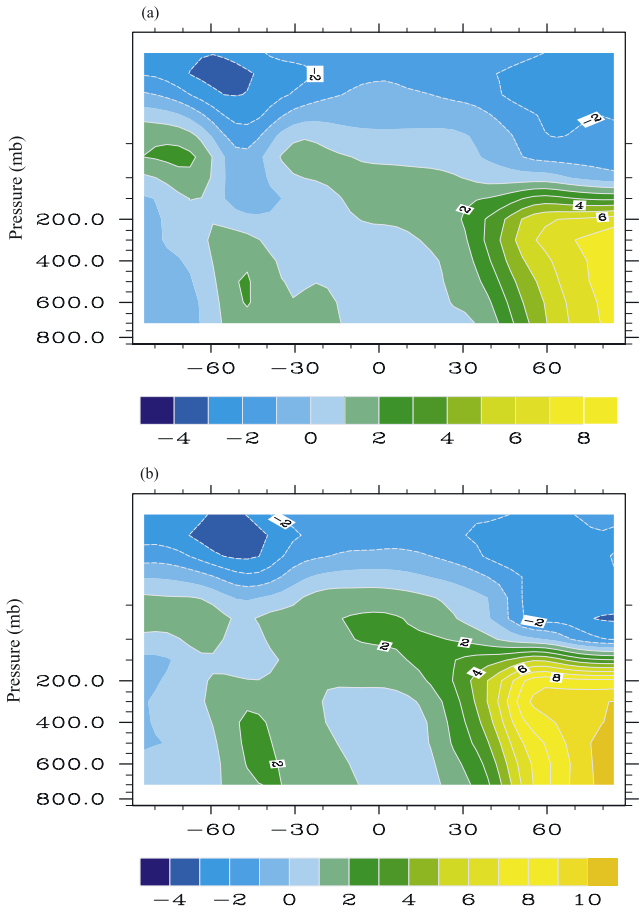

Figure 11. Differences in the July zonal mean temperature (°K) between experiments (a) DUST and CHIN and (b) SOOT and CHIN.

tion distribution in SOOT (the 100% black carbon experiment) also shows decreases in southern and eastern China, as compared to CHIN, with a global reduction of about 0.89 mm d^{-1} in July with respect to CTRL (Table 5). Changes in precipitation are related to the warming in the middle to high latitudes as shown in the perturbed zonal mean temperature (Figure 11b). As a result, precipitation moves to higher latitudes, an effect resembling that of dust aerosols. Similar results have been reported by *Bakan et al.* [1991] who illustrated that the effect of soot aerosols is to increase the heating of the column over the Himalayas and the consequence of shifting precipitation inland. These simulations suggest that the "north drought/south flooding" precipitation pattern that frequently occurred in China during the past 50 years appears to be not directly caused by the black carbon absorption but could be related to the increased aerosol optical depth produced by various anthropogenic sources over the years, as suggested in section 4.3.

5. Conclusions

[37] Climate simulations using an updated version of UCLA AGCM that incorporates a state-of-the-art aerosol/cloud radiation scheme have been carried out to investigate the effects of various types of aerosols on the cloud field, radiation budget, temperature, and precipitation patterns in China and the surrounding areas. In these regions, we have used the aerosol optical depths determined by the Chinese scientists for the past 40 years in the present climate simulations. Key results of our study are summarized in the following.

[38] First, inclusion of a large fraction of maritime aerosols with a uniform optical depth of 0.2 reduces the global mean surface solar insolation by about 5 W m^{-2} due to their scattering and absorption of solar radiation. The positive solar forcing at TOA is associated with reduction in the total cloudiness. The global mean precipitation is reduced by more than 0.3 mm d^{-1}, with decreases found in areas including ITCZ, the East Asian summer monsoon, Central America, and Africa, as a result of the decreased temperature contrast between the tropical area and the middle to high latitudes, which in turn decreases the Hadley circulation leading to reductions in tropical convection and precipitation. The corresponding OLR shows increases in these areas indicating decreased convection. Decreases in the net surface solar radiation and precipitation have corrected the overestimates in the UCLA AGCM simulations without inclusion of the aerosol radiative effect.

[39] Second, increased aerosol concentrations in terms of optical depth in China result in increased simulated precipitation in July in the southern China, Arabian Sea, Bay of Bengal, and Indian areas, where moisture supply is abundant, in conjunction with the increased temperature gradient between the tropical area and midlatitudes. Surface solar fluxes are reduced in most part of China due to the enhanced scattering

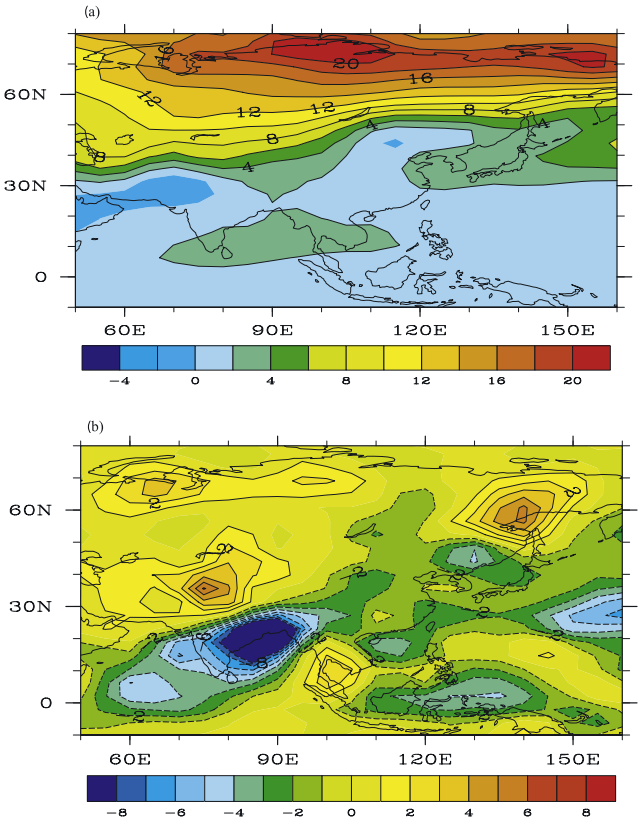

Figure 12. Differences in the July mean (a) surface air temperature (°K) and (b) precipitation (mm d^{-1}) between the experiments SOOT and CHIN.

and absorption related to increased aerosol optical depths. The surface air temperature shows warming to the north of China as a result of decreased cloud cover and increased surface solar insolation in that area. Note that changes in global means are generally insignificant when the aerosol optical depths are increased only in the China region.

[40] Third, aerosol types play an important role in the determination of the global mean radiation budget and regional climate. Sulfates primarily scatter solar radiation, resulting in a reduction in the simulated surface solar flux of more than 7 W m^{-2} in July. The response of regional climate to sulfate aerosols resembles that to maritime aerosols since these two aerosol types have similar single-scattering properties. Large dust particles significantly reduce the solar flux reaching the surface by more than 7 W m^{-2} in July simulations through both scattering and absorption, while positive solar forcing is found at TOA due to substantial absorption. Dust particles also have a significant effect on IR radiation under clear conditions. However, their IR effect in climate simulation is significantly reduced when clouds are present. Large dust particles increase the heating of the atmospheric column of the middle to high latitudes, which weakens the meridional circulation and shifts precipitation landward, e.g., toward the Himalayas such that rainfall occurs over north of the Bay of Bengal. Black carbon aerosols affect both solar and IR radiation mainly through their absorption and the associated effect on cloud fields. The global mean of the simulated solar flux at the surface is reduced by about 18 W m^{-2} in July. Increases in OLR of about 6 W m^{-2} is found in July with respect to the simulated IR radiation in relation to reduced cloud cover and increased surface air temperature. Our simulation results show that the inclusion of black carbon in the model does not produce the ''north drought/south flooding'' precipitation pattern that has frequently occurred in China during the past 50 years.

[41] Finally, it should be noted that the climatic effects of aerosols on the radiative budget, temperature, and precipitation fields are not only produced through their direct radiative forcings, but also through the consequent modulation of the cloud fields formed in the model. This ''indirect'' effect through cloud generated in GCMs could exceed the direct aerosol radiative forcing.

[42] The present study assumes that aerosols are spherical in shape, an assumption that is not valid for mineral dust and black carbon. The nonsphericity of these particles can significantly affect their single-scattering properties and consequently their impact on radiative forcing. It is our plan to develop and parameterize the single-scattering properties of nonspherical aerosols for use in the climate model in order to investigate the radiative forcings of dust particles and black carbon that may deviate from the spherical assumption. We have not yet incorporated the indirect aerosol effect in the UCLA AGCM, a task we plan to accomplish in future endeavors.

[43] **Acknowledgment.** Research reported in this paper has been supported by NSF grants ATM-0437349 and ATM-0331550 and DOE grant DE-FG02-04ER6333724.

References

Alexander, R. C., and R. L. Mobley (1976), Monthly average sea-surface temperatures and ice pack limits on a global grid, *Mon. Weather Rev.*, *104*, 143–148.

Arakawa, A. (2000), A personal perspective on the early years of general circulation modeling at UCLA, in *General Circulation Model Development: Past, Present, and Future—Proceedings of a Symposium in Honor of Professor Akio Arakawa*, edited by D. A. Randall, pp. 1–65, Elsevier, New York.

Bakan, S., et al. (1991), Climate response to smoke from the burning oil wells in Kuwait, *Nature*, *351*, 367–371.

Boucher, O., and T. L. Anderson (1995), GCM assessment of the sensitivity of direct climate forcing by anthropogenic sulfate aerosols to aerosol size and chemistry, *J. Geophys. Res.*, *100*, 26,061–26,092.

Charlock, T. P., and W. D. Sellers (1980), Aerosol, cloud reflectivity and climate, *J. Atmos. Sci.*, *37*, 1136–1137.

Charlock, T. P., F. G. Rose, D. Rutan, Z. Jin, D. Fillmore, and W. Collins (2004), Global retrieval of the surface and atmospheric radiation budget and direct aerosol forcing, paper presented at the Conference on Satellite Meteorology, AMS, Norfolk, U. K.

Chou, M. D., M. J. Suarez, C. H. Ho, M. M.-H. Yan, and K.-T. Lee (1998), Parameterizations for cloud overlapping and shortwave single-scattering properties for use in general circulation and cloud ensemble models, *J. Clim.*, *11*, 202–214.

Chu, D. A., Y. J. Kaufman, C. Ichoku, L. A. Remer, D. Tanré, and B. N. Holben (2002), Validation of MODIS aerosol optical depth retrieval over land, *Geophys. Res. Lett.*, *29*(12), 8007, doi:10.1029/2001GL013205.

Chung, S. H., and J. H. Seinfeld (2005), Climate response of direct radiative forcing of anthropogenic black carbon, *J. Geophys. Res.*, *110*, D11102, doi:10.1029/2004JD005441.

Coakley, J. A., Jr., and R. Cess (1985), Response of the NCAR community climate model to the radiative forcing by the naturally occurring tropospheric aerosols, *J. Atmos. Sci.*, *42*, 1677–1692.

d'Almeida, G. A., P. Koepke, and E. P. Shettle (1991), *Atmospheric Aerosols—Global Climatology and Radiative Characteristics*, 561 pp., A. Deepak, Hampton, Va.

Diner, D. J., et al. (2001), MISR aerosol optical depth retrievals over southern Africa during the SAFARI-2000 dry season campaign, *Geophys. Res. Lett.*, *28*, 3127–3130.

Dorman, J. L., and P. J. Sellers (1989), A global climatology of albedo, roughness length and stomatal resistance for atmospheric general circulation models as represented by the Simple Biosphere model (SiB), *J. Appl. Meteorol.*, *28*, 833–855.

Fu, Q., and K. N. Liou (1992), On the correlated k-distribution method for radiative transfer in nonhomogeneous atmospheres, *J. Atmos. Sci.*, *49*, 2139–2156.

Fu, Q., and K. N. Liou (1993), Parameterization of the radiative properties of cirrus clouds, *J. Atmos. Sci.*, *50*, 2008–2025.

Fu, Q., K. N. Liou, M. C. Cribb, T. P. Charlock, and A. Grossman (1997), Multiple scattering parameterization in thermal infrared radiative transfer, *J. Atmos. Sci.*, *54*, 2799–2812.

Geleyn, J.-F., and A. Hollingsworth (1979), An economical analytical method for the computation of the interaction between scattering and line absorption of radiation, *Beitr. Phys. Atmos.*, *52*, 1–16.

Geogdzhayev, I. V., M. I. Mishchenko, L. Liu, and L. Remer (2004), Global two-channel AVHRR aerosol climatology: Effects of stratospheric aerosols and preliminary comparisons with MODIS and MISR retrievals, *J. Quant. Spectrosc. Radiat. Transfer*, *88*, 47–59.

Ghan, S. J., M. C. MacCracken, and J. J. Walton (1988), Climatic response to large atmospheric smoke injections: Sensitivity studies with a tropospheric general circulation model, *J. Geophys. Res.*, *93*, 8315–8337.

Giorgi, F., X. Bi, and Y. Qian (2002), Direct radiative forcing and regional climatic effects of anthropogenic aerosols over East Asia: A regional coupled climate-chemistry/aerosol model study, *J. Geophys. Res.*, *107*(D20), 4439, doi:10.1029/2001JD001066.

Gu, Y., and K. N. Liou (2001), Radiation parameterization for three-dimensional inhomogeneous cirrus clouds: Application to climate models, *J. Clim.*, *14*, 2443–2457.

Gu, Y., J. Fararra, K. N. Liou, and C. R. Mechoso (2003), Parameterization of cloud-radiation processes in the UCLA general circulation model, *J. Clim.*, *16*, 3357–3370.

Gueymard, C. A., C. N. S. Laulainen, J. K. Vaughan, and F. E. Vignola (2000), China's dust affects solar resource in the U. S.: A case study, paper presented at SOLAR 2000, Proceedings of ASES Annual Conference, U .S. Dep. of Energy, Madison, Wisc., 16–21 June.

Hansen, J., and L. Nazarenko (2004), Soot climate forcing via snow and ice albedos, *Proc. Natl. Acad. Sci. U.S.A.*, *101*, 423–428.

Harshvardhan, A. Arking, M. D. King, and M.-D. Chou (1984), Impact of the El Chichon stratospheric aerosol layer on Northern Hemisphere temperatures, in *Aerosols and Their Climatic Effects*, pp. 261–273, A. Deepak, Hampton, Va.

He, K., F. Yang, Y. Ma, Q. Zhang, X. Yao, C. K. Chan, S. Cadle, T. Chan, and P. Mulawa (2001), The characteristics of $PM_{2.5}$ in Beijing, China, *Atmos. Environ.*, *35*, 4959–4970.

Hess, M., P. Koepke, and I. Schult (1998), Optical properties of aerosols and clouds: The software package OPAC, *Bull. Am. Meteorol. Soc.*, *79*, 831–844.

Kaiser, D. P. (1998), Analysis of total cloud amount over China, 1951–1994, *Geophys. Res. Lett.*, *25*, 3599–3602.

Lefohn, A. S., J. D. Husar, and R. B. Husar (1999), Estimating historical anthropogenic global sulfur emission patterns for the period 1850–1990, *Atmos. Environ.*, *33*, 3435–3444.

Li, D.-M., and K. P. Shine (1995), A 4-dimensional ozone climatology for UGAMP models, *Internal Rep. 35*, UK Univ. Global Atmos. Modell. Program, Reading, UK.

Li, J.-L. F., M. Köhler, J. D. Farrara, and C. R. Mechoso (2002), The impact of stratocumulus cloud radiative properties on surface heat fluxes simulated with a general circulation model, *Mon. Weather Rev.*, *130*, 1433–1441.

Liang, X.-Z., and W.-C. Wang (1997), Cloud overlap effects on general circulation model climate simulations, *J. Geophys. Res.*, *102*, 11,039–11,047.

Liou, K. N., Q. Fu, and T. P. Ackerman (1988), A simple formulation of the delta-four-stream approximation for radiative transfer parameterizations, *J. Atmos. Sci.*, *45*, 1940–1947.

Luo, Y., D. Lu, X. Zhou, W. Li, and Q. He (2001), Characteristics of the spatial distribution and yearly variation of aerosol optical depth over China in last 30 years, *J. Geophys. Res.*, *106*, 14,501–14,513.

Manabe, S., and R. Strickler (1964), Thermal equilibrium of the atmospheres with a convective adjustment, *J. Atmos. Sci.*, *21*, 361–385.

Martins, J. V., P. Artaxo, C. Liousse, J. S. Reid, P. V. Hobbs, and Y. J. Kaufman (1998), Effects of black carbon content, particle size, and mixing on light absorption by aerosols from biomass burning in Brazil, *J. Geophys. Res.*, *103*, 32,041–32,050.

Mechoso, C. R., J.-Y. Yu, and A. Arakawa (2000), A coupled GCM pilgrimage: From climate catastrophe to ENSO simulations, in *General Circulation Model Development: Past, Present, and Future—Proceedings of a Symposium in Honor of Professor Akio Arakawa*, edited by D. A. Randall, pp. 539–575, Elsevier, New York.

Menon, S., J. Hansen, L. Nazarenko, and Y. Luo (2002), Climate effects of black carbon aerosols in China and India, *Science*, *297*, 2250–2253.

Miller, R. L., and I. Tegen (1998), Climate response to soil dust aerosols, *J. Clim.*, *11*, 3247–3267.

Mitchell, J. F. B., T. C. Johns, J. M. Gregory, and S. F. B. Tett (1995), Climate response to increasing levels of greenhouse gases and sulfate aerosols, *Nature*, *376*, 501–504.

Pan, D.-M., and D. A. Randall (1998), A cumulus parameterization with a prognostic closure, *Q.J.R. Meteorol. Soc.*, *124*, 949–981.

Pan, W., A. Tatang, G. J. Mchae, and R. G. Prinn (1997), Uncertainty analysis of direct radiative forcing by anthropogenic sulfate aerosols, *J. Geophys. Res.*, *102*, 21,915–21,924.

Penner, J. E., C. C. Chuang, and K. Grant (1998), Climate forcing by carbonaceous and sulfate aerosols, *Clim. Dyn.*, *14*, 839–851.

Pollack, J. B., D. Rind, A. Lacis, J. E. Hansen, M. Sato, and R. Ruedy (1993), GCM simulations of volcanic aerosol forcing. part I: Climate changes induced by steady-state perturbations, *J. Clim.*, *6*, 1719–1742.

Ramanathan, V., et al. (2001), Indian Ocean experiment: An integrated analysis of the climate forcing and effects of the great Indo-Asian haze, *J. Geophys. Res.*, *106*, 28,371–28,398.

Rayner, N. A., C. K. Folland, D. E. Parker, and E. B. Horton (1995), A new global sea-ice and sea surface temperature (GISST) data set for 1903–1994 for forcing climate models, *Internal Note 69*, 14 pp., Hadley Center, Met Office, Bracknell, U. K.

Remer, L. A., et al. (2002), Validation of MODIS aerosol retrieval over ocean, *Geophys. Res. Lett.*, *29*(12), 8008, doi:10.1029/2001GL013204.

Streets, D. G., S. Gupta, S. T. Waldhoff, M. Q. Wang, T. C. Bond, and B. Yiyan (2001), Black carbon emissions in China, *Atmos. Environ.*, *35*, 4281–4296.

Sun, W. et al. (1997), Variation characteristics of Earth's surface solar radiation in China during 30 recent years, in *Researches for Climate Change in China and its Climatic Effect*, edited by Y. Ding et al., pp. 132–239, Meteorol. Press, Beijing.

Tegen, I., and I. Fung (1995), Contribution to the atmospheric mineral aerosol load from land surface modification, *J. Geophys. Res.*, *100*, 18,707–18,726.

Tegen, I., and A. A. Lacis (1996), Modeling of particle size distribution and its influence on the radiative properties of mineral dust aerosol, *J. Geophys. Res.*, *101*, 19,237–19,244.

Tian, L., and J. A. Curry (1989), Cloud overlap statistics, *J. Geophys. Res.*, *94*, 9925–9935.

Torres, O., P. K. Bhartia, J. R. Herman, and Z. Ahmad (1998), Derivation of aerosol properties from satellite measurements of backscattered ultraviolet radiation: Theoretical basis, *J. Geophys. Res.*, *103*, 17,099–17,110.

Torres, O., P. K. Bhartia, J. R. Herman, A. Sinyuk, and B. Holben (2002), A long term record of aerosol optical thickness from TOMS observations and comparison to AERONET measurements, *J. Atmos. Sci.*, *59*, 398–413.

Wu, J., W. Jiang, C. Fu, B. Su, H. Liu, and J. Tang (2004), Simulation of the radiative effect of black carbon aerosols and the regional climate response over China, *Adv. Atmos. Sci.*, *21*, 637–649.

Xu, J., M. H. Bergin, X. Yu, G. Liu, J. Zhao, C. M. Carrico, and K. Baumann (2002), Measurement of aerosol chemical, physical and radiative properties in the Yangtze delta region of China, *Atmos. Environ.*, *36*, 161–173.

Xu, Q. (2001), Abrupt change of the mid-summer climate in central east China by the influence of atmospheric pollution, *Atmos. Environ.*, *35*, 5029–5040.

Y. Gu, K. N. Liou, C. R. Mechoso, and Y. Xue, Department of Atmospheric and Oceanic Sciences, University of California, Los Angeles, Los Angeles, CA 90095, USA. (gu@atmos.ucla.edu)

W. Li, Chinese Academy of Meteorological Sciences, 46 Zhongguanchun Nandajie, Haidian, Beijing 100081, China.

Y. Luo, Division of Atmospheric Sciences, National Natural Science Foundation of China, Beijing 100085, China.